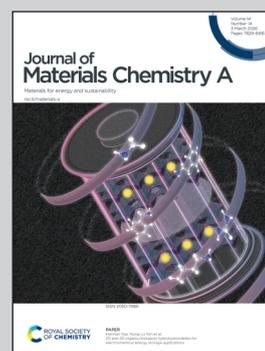**Showcasing research from Professor Jung Woo Lee's laboratory, Department of Materials Science and Engineering, Pusan National University, Busan, Republic of Korea.**

Asymmetric microdome structured flexible and skin-mountable pressure sensors monitored with computational analysis

This cover features a skin-mountable human-motion sensor using large-sized reduced graphene oxide and an asymmetric microdome structure fabricated by facile and cost-effective process. By employing finite element method analysis, the study confirmed that pressure-induced changes in contact points by asymmetricmicrodome structure align with experimental data and practical applications. This robust design enables real-time wireless monitoring of physical activities, positioning the sensor as a critical component for next-generation intelligent wearable devices.

Image reproduced by permission of Jung Woo Lee from *J. Mater. Chem. A*, 2026, **14**, 8041.

As featured in:

See Ki Jun Yu, Sangryun Lee, Jung Woo Lee *et al.*,
J. Mater. Chem. A, 2026, **14**, 8041.

ROYAL SOCIETY OF CHEMISTRY

rsc.li/materials-a

Journal of Materials Chemistry A

PAPER

Check for updates

Asymmetric microdome structured flexible and skin-mountable pressure sensors monitored with computational analysis

Yeoul Kang,†[a] Mary Kim,†[bc] Seung Geun Jo,[a] Jongmoon Jang, [d] Sang-Jin Lee,[e] Ki Jun Yu,*[f] Sangryun Lee *[bc] and Jung Woo Lee *[a]

Flexible pressure sensors are a crucial component in the next generation of wearable electronics. However, the lack of a structural design strategy that can achieve both high sensitivity and a straightforward manufacturing method remains a challenge. This study proposes a novel solution with an asymmetric microdome structure consisting of different radius sizes fabricated by a simple and cost-effective method. Additionally, large-sized reduced graphene oxide is utilized as a sensing material to improve the electrical conductivity by facilitating electron transfer within its large basal plane. The fabricated sensor shows high sensitivity of 63.07 kPa^{-1} up to 0.5 kPa and 1.96 kPa^{-1} in the range of 0.5–10 kPa. The finite element method validates a gradual increase in the number of contact points and area as the applied pressure increases in the asymmetric microdome structure. Moreover, the sensor exhibits a fast response time of 50 ms, excellent repeatability, and mechanical durability over 1000 cycles. Consequently, the sensor is successfully utilized in monitoring the weak radial arterial pulse and detecting various human motions, including wrist bending, phonation, and swallowing activity. The real-time wireless monitoring of daily activities further establishes the sensor's potential for future wearable electronics.

Introduction

Recently, there has been significant progress in the development of wearable electronics designed to seamlessly integrate with the human body, offering convenience in usage regardless of time and place. These advancements are primarily driven by their applications in continuous health monitoring, human–machine interaction, and soft robotics.[1,2] In particular, wearable pressure sensors have gained attention in the healthcare field due to their capability to capture diverse physiological signals, facilitating the diagnosis of health conditions and early disease detection. The pressure ranges associated with human activity can be categorized as follows: ultra-low pressure (<1 Pa) which

rarely occurs in daily activities, the subtle-pressure regime (1 Pa to 1 kPa) for weak biological signals such as pulse wave and respiration, the low-pressure range (1−10 kPa) for daily activities such as gentle touch, manipulation of objects, *etc.*, and the medium-pressure range (10−100 kPa) for pressure of body weight.[3,4] To achieve practicality as wearable devices, accurate data acquisition and high sensitivity within the subtle to low-pressure regime are crucial.[5,6] However, conventional rigid pressure sensors have limitations, including poor wearability and conformability, making it challenging to closely measure physiological signals generated by the body. Flexible pressure sensors can conformally adhere to curved skin, enabling the precise measurement of various physiological signals, such as pulse, respiration, voice, muscle activity, and joint movements.[7,8]

Among the various sensing mechanisms, flexible piezoresistive pressure sensors have been extensively developed due to their simple structure, readout mechanism, and fast response.[9,10] Typically, they consist of a conductive material coated on two interlocked elastomer substrates. The sensing mechanism involves an increase in pressure, leading to an increase in the contact area between conductive layers, resulting in an increased conductive pathway, thus changing the total current of the sensor. Since the sensitivity of the sensor is defined as the relative current change under applied pressure, change in the contact area with pressure plays a crucial role in

[a]*Department of Materials Science and Engineering, Pusan National University, Busan, 46241, Republic of Korea. E-mail: jungwoolee@pusan.ac.kr*

[b]*Department of Mechanical and Biomedical Engineering, Ewha Womans University, Seoul 03760, Republic of Korea. E-mail: sr.lee@ewha.ac.kr*

[c]*Graduate Program in System Health Science and Engineering, Ewha Womans University, Seoul 03760, Republic of Korea*

[d]*Department of Electronic Engineering, Yeungnam University, Gyeongsan, 38541, Republic of Korea*

[e]*School of Semiconductor Engineering, Chungbuk National University, Cheongju, 28644, Republic of Korea*

[f]*School of Electrical and Electronic Engineering, Yonsei University, 50 Yonsei-ro, Seodaemungu, Seoul 03722, Republic of Korea. E-mail: kijunyu@yonsei.ac.kr*

† These authors contributed equally to this work.

determining the sensor's sensitivity. Previous research efforts have involved introducing microstructured elastomer surfaces, such as pyramids,[11,12] domes,[13,14] or cylinders,[15,16] to enhance sensitivity by inducing stress concentration at small contact points, leading to easy deformation. However, there remains a persistent limitation in sensitivity because the contact area increases rapidly and reaches a saturation point due to stress accumulation at the single contact point. Therefore, recent research has focused on structures that allow sequential changes in contact area, starting from a smaller initial contact area.

In this regard, microstructures with a complex surface have been introduced to enable a progressive increase in the number of contact regions with increasing pressure.[17–19] For example, Shi *et al.* utilized lotus leaf replication, which possesses a hierarchical structured surface with nanostructures on the microstructure.[20] With increasing pressure, the microstructures deform, simultaneously increasing the number of contacting nanostructures, resulting in a high sensitivity of 1.2 kPa^{-1} under a pressure of 25 kPa. Li *et al.* fabricated the hierarchical architecture inspired by the snails, using a multi-step laser process to make each cylindrical column, tentacle-like conical pillar, and porous dome.[21] As the pressure increased, each structure sequentially deformed, showing remarkable sensitivity of 35.51 kPa^{-1} under a pressure of 0.25 kPa. While these structures have improved sensing properties compared to simple surface structures, they still have limitations in terms of structural consistency and require multi-step manufacturing procedures. For practical applications, an innovative structure that can provide high sensitivity through a simple and scalable fabrication method is needed.

In this study, we present a novel approach to address these challenges by proposing an asymmetric microdome structure (AMS) pressure sensor composed of interlocked microdome structures with different radius sizes, eliminating the need for complex surface manufacturing. When a larger microdome structure on the top layer, responsible for load transfer, comes into contact with a smaller microdome structure on the bottom layer, it can have a smaller initial contact area per unit area compared to symmetric microdome structures (SMSs), which consist of interlocked microdome structures with the same radius size. As the pressure increases, the microdomes compress gradually, leading to an increase in the contact area at the initial contact point and, simultaneously, making new contact points with adjacent bottom microdomes. This leads to a greater rate of contact area change, allowing for a higher sensitivity of the sensor. Utilizing patterned molds for microstructure fabrication ensures consistency in design and dimensions and enhanced efficiency and scalability of production.[22,23] Additionally, we adopted a cost-effective approach, isotropically etched copper foil molds to fabricate microdome-textured PDMS (md-PDMS), enabling an economical process that avoids the vacuum-based dry etching required in conventional Si-wafer-based microfabrication. The sensing material integrated with the md-PDMS surface should exhibit significant changes in the electronic conduction path as the contact area increases.[24,25] Large-sized reduced graphene oxide (LrGO) with

a large basal plane and low intersheet junctions can facilitate electron transfer.[26,27] Furthermore, LrGO provides advantages such as compatibility with cost-effective solution processes and excellent mechanical properties inherent to carbon materials. Moreover, its 2D structure makes it well-suited for conformal coating on microstructures, offering advantages over 0D materials and 1D materials.[28,29] By combining an effective structure with the suitable sensing material, the sensor demonstrates impressive sensing properties. The sensing effect of AMS is also validated through theoretical calculations by employing the finite element method (FEM). With their superior properties, it can detect finger pressing and dynamic signals such as acoustic vibration in loudspeakers. Additionally, the sensor with high sensitivity in the subtle to low-pressure range successfully detected the wrist pulse and muscle and joint movements. Furthermore, the real-time wireless monitoring through mobile apps makes these sensors promising components for wearable applications.

Results and discussion

Fig. 1a shows an AMS pressure sensor incorporated in an md-PDMS substrate with a thickness of ~500 μm, responsible for surface structure formation, and radii of 50 and 10 μm in the top and bottom layers, respectively, conformally coated with an LrGO layer of ~62 nm thickness. Under the applied pressure, conductive pathways are established in the contact region between the top and bottom LrGO layers, resulting in the output of the current value. The sensor affixed to various parts of the body can utilize wireless data transmission to enable unrestricted real-time monitoring of human motion and physiological signals based on the obtained output value. Fig. 1b demonstrates the working mechanism of the pressure sensors, where the contact area change process occurs as the pressure increases, which is directly related to the sensitivity of the sensor. SMSs have a limited variation in contact area owing to rapid stress accumulation at the initial contact point with increasing pressure. In contrast, AMS initiates from a small initial contact area due to the small radius of the microdome in the bottom layer and the lower number of contact points per unit area. Under high pressure, additional contact points emerge, as confirmed in Fig. 1c, enabling a sequential increase in the contact area. Consequently, this enhancement in the contact area variation ultimately leads to an enhancement of the sensitivity. Furthermore, for wearable sensors, it is crucial to conformally adhere to the skin to accurately capture weak biosignals, such as pulse signals. The fabricated sensor, with a PDMS substrate of about 500 μm thickness coated with LrGO, demonstrated excellent mechanical flexibility, allowing it to conformally attach to curved skin such as the wrist (Fig. 1d). Fig. 1e demonstrates the measurements of the radial artery pulse in a normal state and immediately after exercise. In comparison to the normal state, there is a significant change in the pulse rate and pulse waveform after exercise. This indicates that the sensor, with its high sensitivity and conformal attachment to the skin, can accurately and reliably detect
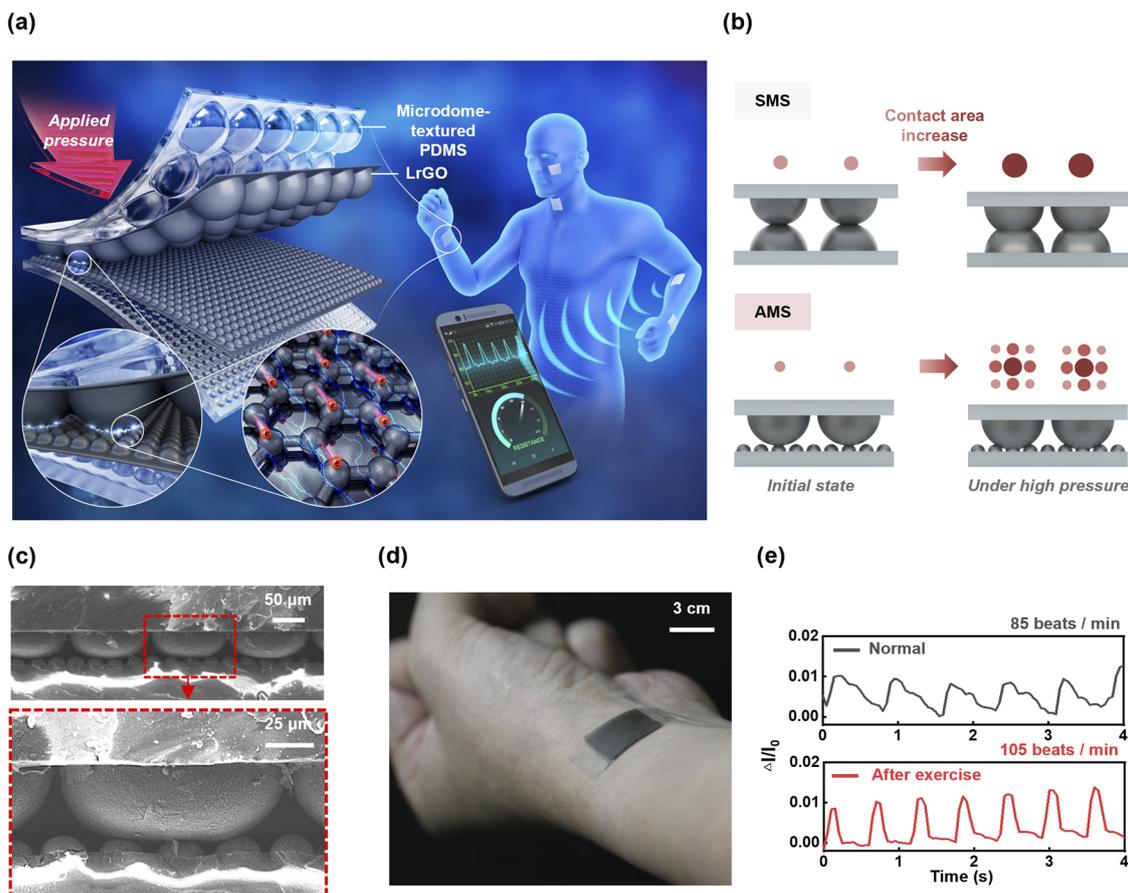
8042 | *J. Mater. Chem. A*, 2026, **14**, 8041–8051

This journal is © The Royal Society of Chemistry 2026

Fig. 1 Graphical representations and images of the AMS pressure sensor. (a) Schematic illustration of the AMS pressure sensor and the electron transfer in the contact region under applied pressure. (b) Concept of contact area variation as the pressure increases in the SMS (top) and AMS (bottom). (c) Cross-sectional SEM image of the AMS pressure sensor under compressive force. (d) Optical image of the AMS pressure sensor mounted on the wrist. (e) Pulse waveform measurements in the normal state (top) and after exercise (bottom).

physiological signals during variations in health conditions, confirming its suitability as a wearable device.

Large-sized graphene oxide (LGO) was synthesized using the modified Hummers' method, employing expanded graphite to facilitate the penetration of the oxidizer solution between the graphite layers, preventing the crack formation of the GO sheets.[30,31] The synthesized LGO sheet exhibited a large lateral dimension >100 μm (Fig. 2a), and an average size of 2710 μm^2, significantly larger than small-sized graphene oxide (SGO) with an average size of 1.333 μm^2 (Fig. 2b and S1). As described in Fig. 2c, after chemical reduction, LrGO had a sheet resistance of 526 ± 82 Ω sq^{-1}, which was lower than that of SrGO of 2122 ± 106 Ω sq^{-1}. The md-PDMS was fabricated by pouring the PDMS mixture onto the copper-based mold with negative hemisphere pattern arrays, as shown in Fig. S2. Subsequently, the LGO solution was spray-coated onto md-PDMS, followed by chemical reduction to form LrGO/md-PDMS with an LrGO thickness of < 62 nm (Fig. S3 and S4). Fig. 2d and S5 display the image of LrGO/md-PDMS, revealing distinct color change from clear md-PDMS to light yellow LGO/md-PDMS and dark brown LrGO/md-PDMS,[32,33] confirming its uniform coating over the entire md-PDMS substrate. Furthermore, the coverage of the LrGO coating layer on the md-PDMS substrate indicates that the LrGO

layer was conformally coated along the contours of the md-PDMS surface, allowing for more reliable sensing of mechanical deformations (see Fig. 2e and S6). Fig. 2f shows the Raman spectra of md-PDMS, LGO/md-PDMS, and LrGO/md-PDMS. For the bare md-PDMS substrate, there were four characteristic peaks around 1264, 1411, 2908, and 2965 cm^{-1}, corresponding to the symmetric bending, asymmetric bending, symmetric stretching, and asymmetric stretching of CH$_3$, respectively.[34] On the other hand, the Raman spectra of both LGO/md-PDMS and LrGO/md-PDMS exhibited two distinct peaks of the carbon-based materials: a D band at 1340 cm^{-1} and a G band at 1580 cm^{-1}. The D band indicates disorder in the graphitic structure, and the G band originates from in-plane bending motion of the C–C bond, representing the degree of structural order. After reduction, the intensity ratio of the D band and G band (I_D/I_G) increased from 0.98 to 1.10, indicating a decrease in the average size of the sp^2 domains, which results from an increase in the number of sp^2 domains.[35,36] This suggests that the reduction process increases the isolated graphene domain due to the removal of oxygen-containing functional groups from LGO.[37] As a result, LrGO had been successfully reduced from LGO, leading to the restoration of its electrical conductivity. As depicted in Fig. S7, both LrGO/md-PDMS substrates for the top
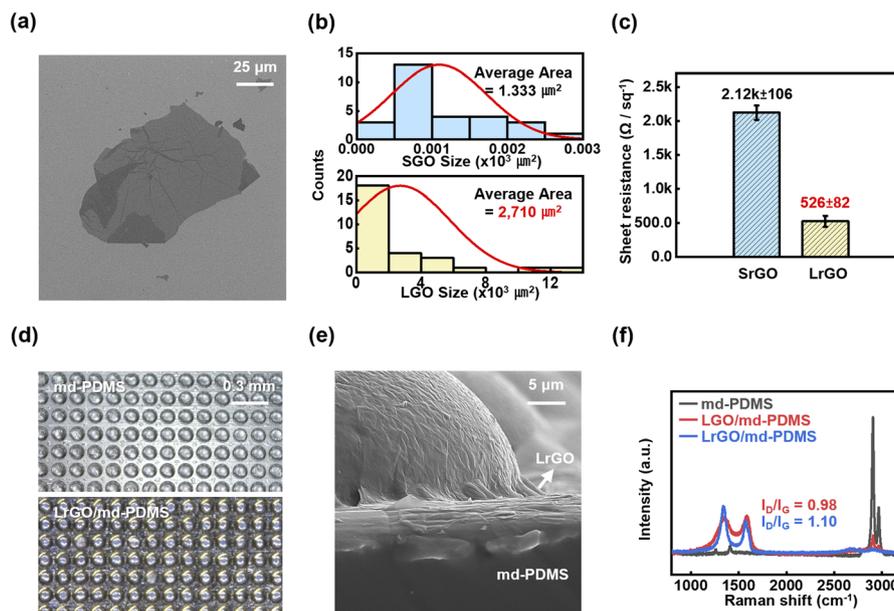
This journal is © The Royal Society of Chemistry 2026

J. Mater. Chem. A, 2026, **14**, 8041–8051 | **8043**

Fig. 2 Characterization of materials and geometries. (a) SEM image of a single LGO sheet. (b) Areal distribution of the SGO and LGO sheets from SEM images. (c) Sheet resistance of LrGO and SrGO. (d) Optical images of md-PDMS without LrGO coating (top) and with LrGO coating (bottom). (e) Cross-sectional SEM image of LrGO-coated md-PDMS with a radius of 50 μm. (f) Raman spectra of md-PDMS, LGO/md-PDMS, and LrGO/md-PDMS.

and bottom layers of AMS were successfully fabricated. Consequently, the above results indicate that LrGO, fully coated on the md-PDMS surface, can provide a more extensive conductive pathway for electron transfer within its structure under applied pressure compared to SrGO.

Sensitivity of pressure sensors

To evaluate the performance of the pressure sensor, the sensitivity (S) was calculated using the following equation:

$$S = (\Delta I/I_0)/\Delta P \tag{1}$$

where I_0 and ΔI represent the initial current without applied pressure (P) and the current variation under the applied pressure, respectively. Prior to the discussion of the piezoresistive sensing performance of the AMS, we investigated the sensitivity enhancement of sensors with microstructured surfaces compared to flat surfaces. First, the radius of the largest radius microdome used for the top layer was fixed with the experimental size limit of radius as 50 μm, which could be obtained from the isotropic etching process. Compared to the planar structure cases with two flat layers (flat + flat) and the single microdome structure layer on top of the flat bottom layer (50 + flat), the interlocked microdome structure consisting of two microdome structures with 50 μm radius (50 + 50) exhibited the highest sensitivity (Fig. S8). These results demonstrate that the microstructure can dramatically enhance sensitivity, which can be attributed to its high compressibility, resulting in significant deformations under pressure.[38] We also explored the effect of the asymmetry ratio in the interlocked microdome structure. The asymmetry ratio could be increased as the radius of the microdome in the bottom layer was decreased to 10 μm, which

was the minimum radius achievable with the resolution of our photolithography system. This increase results in a smaller initial contact area and a greater number of maximum contact points at high pressure, as depicted in Fig. S9a, resulting in an increased relative contact area change and sensitivity (Fig. S9b). Therefore, we aimed to experimentally verify the improvement in pressure sensing performance of the AMS with an asymmetry ratio of 5.

Fig. 3a demonstrates the relative current ($\Delta I/I_0$) variation of the sensors under applied pressure, using AMS with different radii of 50 μm and 10 μm for individual top and bottom layers, as well as SMS (L) and (S) with the same size of radius in both top and bottom layers in 50 μm and 10 μm, respectively. As depicted in Fig. 3b, the AMS pressure sensor exhibited a sensitivity of 63.07 kPa^{-1} under 0.5 kPa, which is approximately 4−5 times higher than the sensitivities of the SMS (L) and (S) pressure sensors, which are 12.96 kPa^{-1} and 15.88 kPa^{-1}, respectively. In the high-pressure range (0.5–10 kPa), the AMS pressure sensor showed a sensitivity of 1.96 kPa^{-1}, almost 6 times higher than that of the SMS (L) and (S) pressure sensors with values of 0.30 kPa^{-1} and 0.33 kPa^{-1}, respectively.

For the sensing material, the AMS pressure sensor using SrGO exhibited lower current variation and sensitivity compared to LrGO, as shown in Fig. S10. This indicates that the flow of current is restricted under increased applied pressure when the sensing material has high resistance. Notably, the AMS pressure sensor with an LrGO coating demonstrated higher sensitivity than the sensor coated with Ag (Fig. S11). The Ag conductive layer, with a sheet resistance of 0.8 Ω, shows a consistently high current value for the overall pressure range, indicating that the electrical response is dominated by bulk resistance. As a result, changes in contact resistance contribute
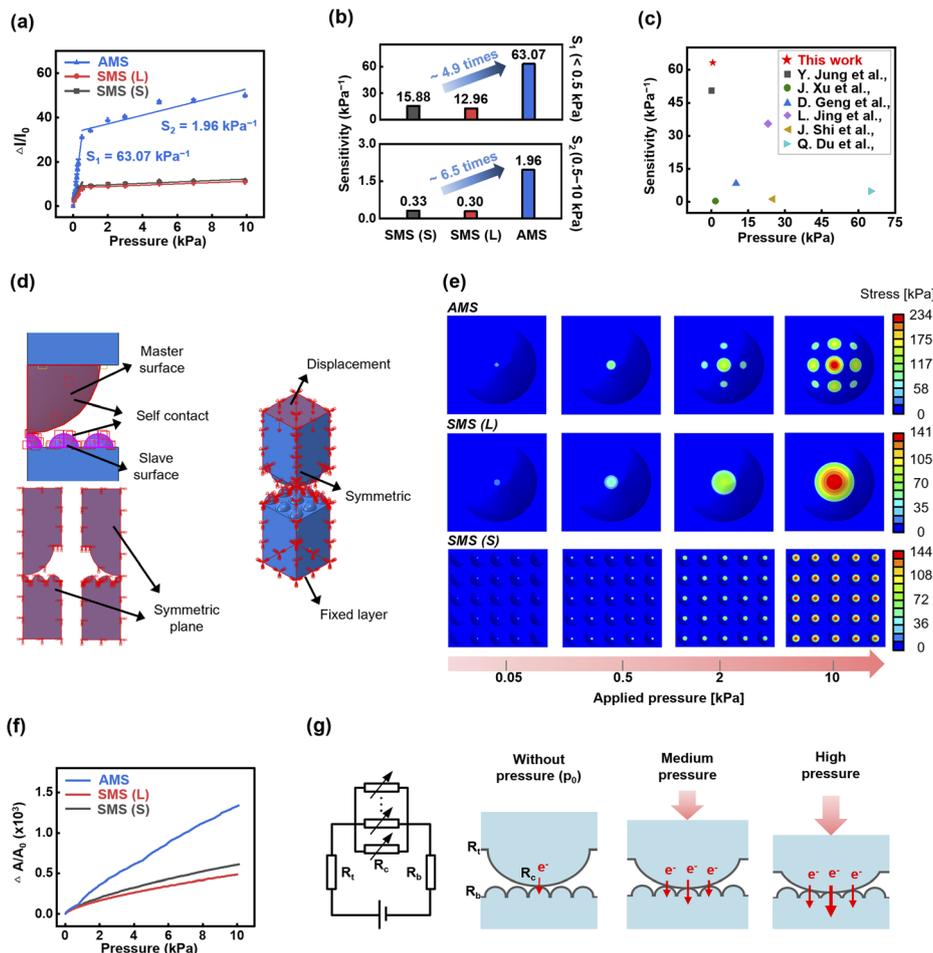
8044 | *J. Mater. Chem. A*, 2026, **14**, 8041–8051

This journal is © The Royal Society of Chemistry 2026

Fig. 3 Experimental, FEM simulation, and circuit modeling analysis of the pressure sensors. (a) $\Delta I/I_0-P$ curves of the AMS and SMS pressure sensors and (b) sensitivity values of the AMS and SMS pressure sensors in low (<0.5 kPa) and high (0.5–10 kPa) pressure ranges. (c) Comparison of the maximum sensitivity of flexible piezoresistive sensors with microstructures in different pressure ranges. (d) FEM model of the AMS with the boundary condition. FEM results on (e) the contact pressure distribution and (f) the relative contact area variation of the AMS and SMS pressure sensors with increasing applied pressure. (g) Proposed circuit model and sensing mechanism of the AMS pressure sensor.

minimally to the overall response, leading to a small relative current change ($\Delta I/I_0$). Consequently, these results represent that LrGO can potentially replace the metal deposition processes involving high vacuum conditions with a cost-effective solution process while enhancing the performance of the proposed sensor through appropriate electrical conductivity. In terms of structural design, recently developed piezoresistive sensors have been introduced with intricate surface structures to enable sequential change in the contact area. In contrast, the AMS pressure sensor demonstrated superior sensitivity compared to recently developed sensors by incorporating LrGO and a simpler structure without the need for any surface processing (Fig. 3c and Table S1).

Computational analyses of contact area variation in AMS and SMS

For further theoretical investigation, FEM was introduced to verify the behavior of the contact area change through deformation under compressive loading. As shown in Fig. S12, the

microdomes were modeled with the same radius size used in the experiment and placed on a substrate with a side length of 125 μm and a height of 100 μm. After generating the microstructure geometry, the FEM was conducted following the procedure depicted in Fig. S13a. Since stress concentration occurs at the contact surface of the microdome, small elements were used near the microdome to construct a fine mesh, as shown in Fig. S13b. For the boundary conditions, the lower surface of the bottom part was fixed, and a displacement of 150 μm was applied to the upper surface of the top part in a downward direction. Therefore, the top part presses the bottom part fixed to the bottom surface, and a total of three contact pairs (top part-bottom part, self-contact in top part, and self-contact in bottom part) were considered (Fig. 3d and S13c). Contact pressure distributions were predicted under the same applied pressure condition, and the relative contact area variation was calculated. When the compressive pressure was applied, stress occurred on the contact surface of the microdome, as demonstrated in Fig. 3e. In the initial state, the AMS exhibited the smallest initial contact area among the three structures. With

This journal is © The Royal Society of Chemistry 2026

J. Mater. Chem. A, 2026, **14**, 8041–8051 | **8045**

increasing pressure, the initial contact area increases, and simultaneously, the number of compressed microdomes in the bottom layer increases. On the other hand, in the SMSs, the microdomes of the top part and the bottom part are in contact with each other at a ratio of 1 : 1 independent of the radius size, and stress occurs at a single contact point. This explains the observed experimental results, where SMS pressure sensors with varying radius sizes exhibited similar values in relative current variations, as shown in Fig. S14. Since the number of microdomes does not increase with loading, a large force is required to increase the contact area. As a result, the AMS showed a larger relative contact area variation than the SMSs under the same applied loading (Fig. 3f). Accordingly, the consistency between the FEM-predicted contact area change and the experimentally observed sensitivity trends suggests that the sensor response is primarily determined by the designed contact formation mechanism.

Equivalent circuit analysis of the pressure sensor

To investigate the relationship between contact area change and resistance variation under applied pressure, a simple circuit model of the sensor was established, as depicted in Fig. 3g. The total resistance of the pressure sensor (R_{total}) can be expressed as the sum of the contact resistance between the microstructures ($R_{contact}$) and the series resistance of the conductive layer (R_{series}), which can be described as follows:

$$R_{total} = R_{contact} + R_{series} = \cfrac{1}{\cfrac{1}{R_{c_1}} + \cfrac{1}{R_{c_2}} + \cdots + \cfrac{1}{R_{cn}}} + R_t + R_b \quad (2)$$

where R_t and R_b are the resistance values of the top and bottom conductive layers, respectively. $R_{contact}$ can be obtained by the parallel circuit of the single contact resistance (R_{ci}) at each contact point i, while n is the number of microstructures in contact between top and bottom layers. R_{series} is composed of the series resistance and R_b. According to Holm's theory,[39,40] R_{ci} can be expressed as a function of contact area as follows:

$$R_{ci} = \frac{\rho}{2a_i} = \frac{\rho}{2}\left\{\frac{\pi}{A_{ci}}\right\}^{1/2} \quad (3)$$

where ρ is the electrical resistivity and a is the radius of the circular contact area at contact point i ($A_{ci} = \pi a_i^2$).

By considering the effect of the applied pressure (ρ) on the contact area, the function of the contact area can be represented as $A_{ci}(p)$.

Therefore, the total resistance of the sensor under the applied pressure can be expressed as follows:

$$R_{total}(p) = \frac{2}{\rho\sqrt{\pi}} \frac{1}{\sqrt{A_{c_1}(p)} + \sqrt{A_{c_2}(p)} + \cdots + \sqrt{A_{cn}(p)}} + R_t + R_b \quad (4)$$

As depicted in Fig. S15, in the pressure state (i) for AMS, the initial contact area $A_{ci}(p_0)$ increases with growing pressure, starting from a small value. As the pressure increases over the state (i), new A_{ci} values are added, providing non-saturated

contact areas for increasing pressure to states (ii) and (iii). In contrast, SMSs have a constant value of n, with only the existing A_{ci} increasing, and the growth rate of the contact area decreasing with increasing pressure. Consequently, the AMS pressure sensor can exhibit a higher relative current variation under the applied pressure compared to the SMS pressure sensors, which demonstrates the high sensitivity observed in the experiment. While the AMS pressure sensor consistently showed the highest relative changes in both theoretical contact area and experimental current values, the decrease in sensitivity at high pressure (>0.5 kPa) in experiments for all structures can be attributed to the existence of inherent R_{series}.[41,42] To clarify, in the low-pressure range, where $R_{contact} \gg R_{series}$, the current variation is primarily dependent on the reduction in $R_{contact}$. However, when $R_{contact}$ becomes significantly small and the influence of R_{series} on R_{total} becomes substantial, the degree of increase in total current decreases. Nevertheless, it is evident that AMS can enhance sensing performance throughout the entire pressure range, highlighting the significance of this study.

We further evaluated the sensing characteristics of the AMS pressure sensor. As shown in Fig. 4a, the sensor exhibited stable and reliable responses under repeated pressures of 0.1, 0.2, 0.5, 2, and 5 kPa. Fig. 4b represents that the sensor has rapid response and recovery times of 50 and 100 ms, respectively, which are crucial for real-time monitoring in the high-speed dynamic changes. The longer recovery time can be attributed to the inherent viscoelastic recovery properties of the PDMS substrate.[43] Furthermore, the sensor demonstrated the capability to detect subtle pressures such as 17 Pa for rice grains and weak air blowing through the mini blower (Fig. 4c and d). This result suggests that the device is well-suited for applications requiring sensitive detection within an extremely low-pressure range. In addition, to investigate the robustness of the device, the cycling stability test was conducted by applying repeated loading/unloading pressures of 0.5 and 10 kPa, respectively. The sensor demonstrated excellent mechanical stability, with no significant degradation of current variation observed during 1000 cycles, as shown in Fig. 4e and f. These results indicate the outstanding reliability and durability of the AMS pressure sensor, which can contribute to long-term usage.

Combining remarkable sensitivity to subtle pressure changes with repeatable, fast, and stable response capabilities, the AMS pressure sensor had remarkable versatility across a wide range of practical applications. As shown in Fig. 5a, the sensor could immediately detect the minute changes in applied finger pressure owing to its high sensitivity and rapid response time. Moreover, as demonstrated in Fig. 5b, the sensor exhibited the ability to detect both short and long pressure signals through finger touch, converting them into Morse code signals for specific words like "SOS" and "PNU." Furthermore, the sensor could effectively detect dynamic signals based on its rapid response time. When attached to a loudspeaker, the sensor could generate distinct current patterns for three specific words, "Flexible", "Pressure", and "Sensor", produced by acoustic vibrations (Fig. 5c). The decrease in the output current values of the sensor may be attributed to the irregular
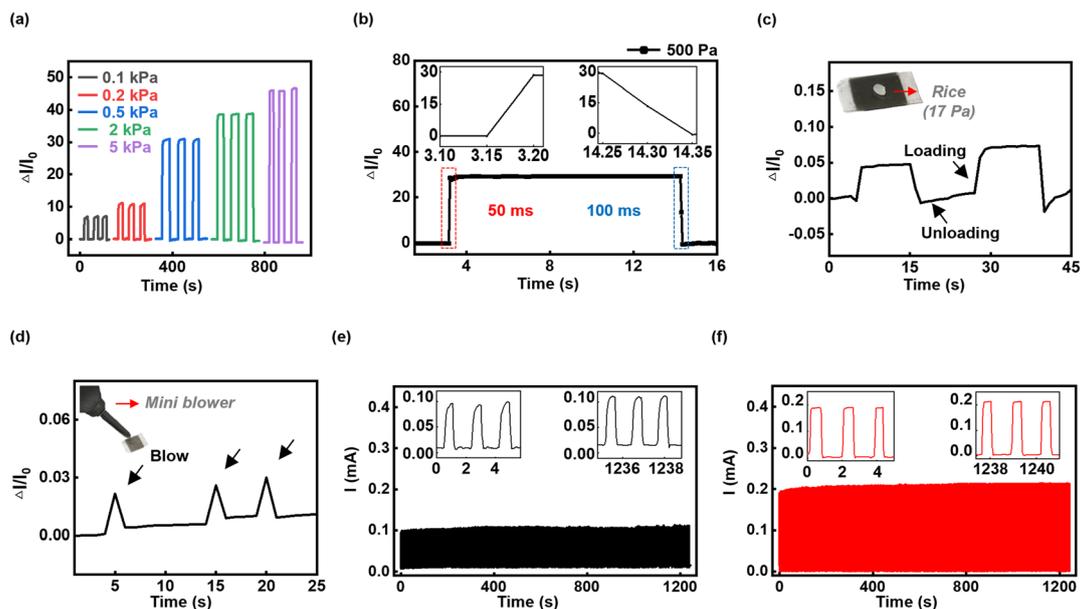
8046 | *J. Mater. Chem. A*, 2026, **14**, 8041–8051

This journal is © The Royal Society of Chemistry 2026

Fig. 4 Sensing performance of the AMS pressure sensor. (a) $\Delta I/I_0-T$ curves in response to different pressures. (b) Response and recovery time of the sensor with an applied pressure of 500 Pa. (Inset) Magnified views of the response (left) and recovery (right) curves (c) Detection of a lightweight object (*i.e.*, rice grain). of 17 Pa. (Inset) An optical image of the rice grain placed on the sensor. (d) Detection of air blowing by a mini blower. (Inset) An optical image of the mini blower located 2 cm above the sensor. Cycling stability tests up to 1000 cycles under (e) 0.5 kPa and (f) 10 kPa, respectively. (Inset) Magnified views of the current plot during the first 3 cycles (left) and last 3 cycles (right).
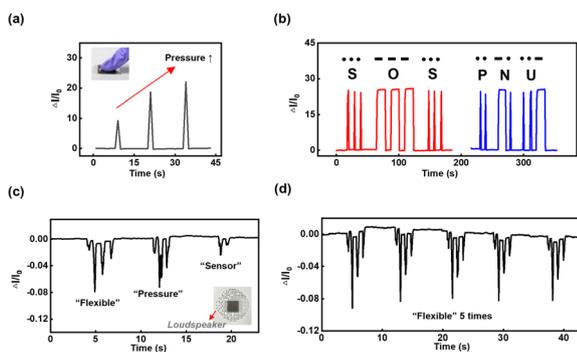

Fig. 5 Sensing capabilities of the AMS pressure sensor in human-machine interface applications. (a) Response of the sensor to different pressures from finger pressing. (Inset) An optical image of the index finger pressing on the sensor. (b) Temporal and static signals generated by finger pressing with different durations, representing Morse code signals "SOS" and "PNU". Response of the sensor to (c) acoustic vibration from a loudspeaker and (d) a 5 times repeated phrase "Flexible". (Inset) An optical image of the sensor attached to the loudspeaker.

directional pressure generated during acoustic vibrations, leading to reduced contact between the layers.[44–46] Fig. 5d presents that the sensor could also exhibit stable and repeatable characteristic peaks for 5 times repeating the word "Flexible". The ability to resolve these signals without observable signal overlap or distortion indicates that the sensor's response and recovery characteristics are sufficient to follow relatively high-frequency pressure variations.

Therefore, the AMS pressure sensor has validated its potential for sensitive touch detection, message transmission, and

sound recognition, which shows promising capabilities for the wearable device in the broad field of human–machine interaction.

When the AMS pressure sensor is mounted on the curved skin, it can be applied to detect physiological signals and human motions from various parts of the body for health monitoring with its superior sensitivity in a wide pressure range of 10 kPa, where general human activities include. Blood pulse is one of the fundamental physiological signals required for diagnosing health conditions, which produce a weak pressure of 1 Pa to 1 kPa.[4] Monitoring the pulse intensity, waveform, and frequency is essential for preventing and diagnosing cardiovascular diseases.[47,48] The AMS pressure sensor exhibited higher sensitivity in the low-pressure range of <0.5 kPa compared to the sensors presented in previous research measuring the wrist pulse, enabling a clear distinction of pulse waveforms.[21,57] As shown in Fig. 6a, three distinguishable characteristic peaks in a single waveform were observed: systolic peak pressure (P_1), late systolic peak pressure (P_2), and diastolic pulse waveform (P_3).[49] After exercise, the pulse waveform exhibited a shorter period and a distinct change in the pulse waveform due to exercise-induced dilation of vasodilation and muscular arteries (Fig. 6b).[50]

The motion recognition capabilities of the sensor significantly expand its range of health monitoring applications to assist in rehabilitation, sports, and medical diagnosis.[51–53] Assessing the range of motion in specific joints is crucial for understanding joint health. When attached to the wrist joint, the sensor effectively distinguished bending movements (Fig. S16a). As shown in Fig. 6c, the sensor also exhibited distinct changes in output signal intensity corresponding to
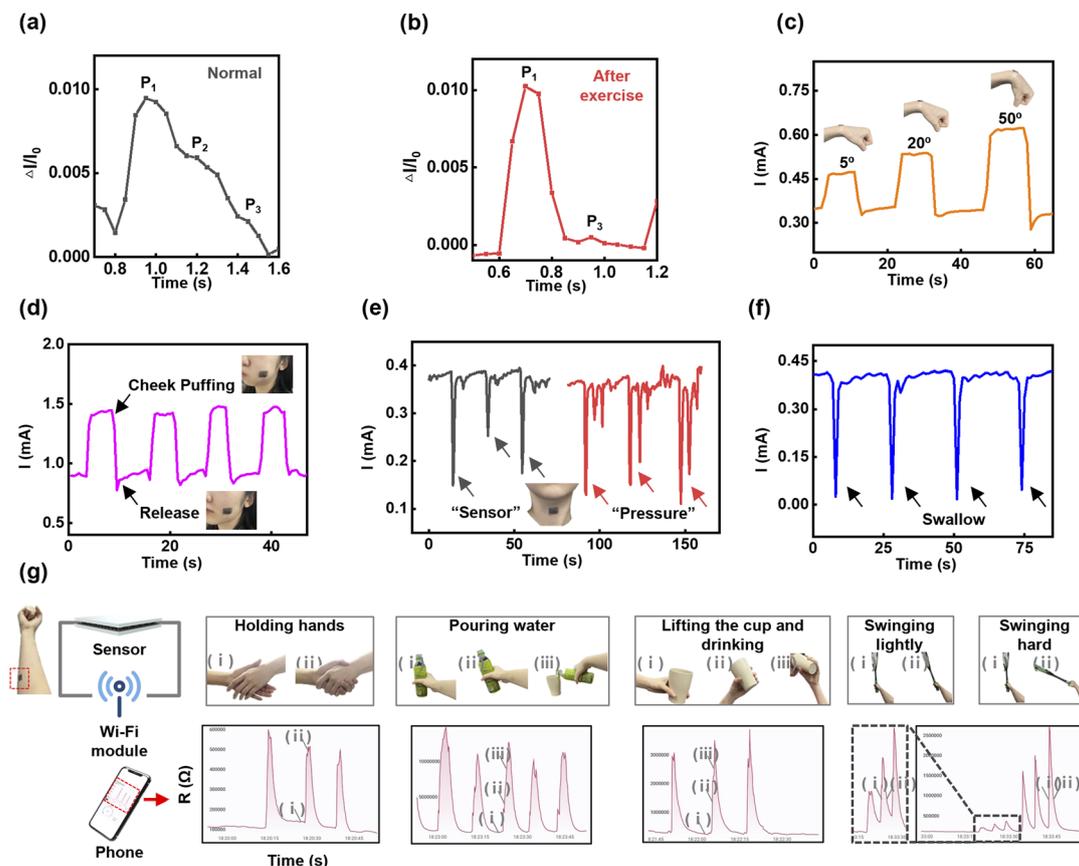
This journal is © The Royal Society of Chemistry 2026

J. Mater. Chem. A, 2026, **14**, 8041–8051 | **8047**

Fig. 6 Physiological signals and human motion monitoring with the AMS pressure sensor. Single pulse waveform in the (a) normal state (b) and after exercise. Response of the sensor to various physiological activities of (c) wrist bending with increasing wrist bending angles – (inset) an optical image of the sensor attached to the wrist joint; (d) cheek puffing – (inset) an optical image of the sensor attached onto the cheek; (e) voice of repeated phrases – (inset) an optical image of the sensor attached to the Adam's apple; (f) swallowing. (g) Wireless real-time monitoring of various daily activities by the sensor attached to the forearm muscle using a mobile application.

different bending angles. This demonstrates the sensitivity of the sensor to subtle changes in joint movements, enabling the quantitative evaluation of joint mobility, contributing to the prevention of arthritis.

As shown in Fig. S16b, when mounted on the back of the hand, the sensor exhibited distinct current changes in response to hand grasping actions as contraction and relaxation of muscles, indicating its potential for gesture recognition and prosthetic limbs.[54] Additionally, Fig. 6d demonstrates that the sensor could detect facial muscle movements, such as cheek puffing, suggesting its potential to detect facial paralysis. Moreover, the sensor attached to the Adam's apple could monitor muscle movements associated with phonation and swallowing activity. Repeatable characteristic peaks for the pronunciation of "sensor" and "pressure" were observed, as shown in Fig. 6e, indicating its applicability in voice recognition. The sensor also demonstrated the capability to recognize swallowing actions (Fig. 6f), which can aid in diagnosing dysphagia and monitoring its progress.[55] For practical applications of wearable devices, wireless measurements are crucial to ensure unrestricted movement. Therefore, we demonstrated a wireless transmission system connecting the sensor to a smartphone (Fig. S17). When attaching the sensor to the

forearm muscle, this system successfully monitored resistance changes as muscles contracted and relaxed during various daily activities, including holding hands, pouring water, lifting a cup and drinking, and swinging a tennis racket gently or forcefully in real-time through a mobile app, as depicted in Fig. 6g and Video S1.

All demonstrations were conducted under direct skin contact, where local humidity variations are present, and stable signal characteristics were consistently observed without noticeable baseline drift. Additionally, the stable and repeatable responses observed at the single-element level indicate that the proposed sensor architecture can be extended to array configurations. Array-level integration, including spatial resolution and multiplexed signal processing, and practical applications, such as vascular pressure mapping, human motion detection, or touch-screen responses, can be addressed in future studies based on the unit-cell platform established in this work.

Conclusions

In this study, instead of the previous structure with a sophisticated surface, the AMS was employed by interlocking the microdome structure with different radius sizes to improve the

8048 | J. Mater. Chem. A, 2026, 14, 8041–8051

This journal is © The Royal Society of Chemistry 2026

sensitivity. Additionally, LrGO was utilized as an excellent sensing material, providing enhanced electrical conductivity with conformal coating on the microstructure. The fabrication process adopted a cost-effective and scalable approach, using a copper-based patterned mold and a spray-coating method. The AMS pressure sensor demonstrated significantly higher sensitivity of 63.07 kPa^{-1} under 0.5 kPa and 1.97 kPa^{-1} in the range of 0.5–10 kPa, which were up to 6 times higher than those of SMSs. Furthermore, experimental results were validated by examining the behavior of contact area change under compressive loading through numerical analysis with FEM simulation. Due to the generation of new contact points and the sequential increase of the contact area, AMS exhibited the highest rate of contact area variation compared to other SMSs, which can be attributed to high sensitivity. The AMS pressure sensor also showed excellent repeatability, response time, and durability. With these superior sensing properties, the sensor demonstrated practical applications in human–machine interfaces, such as sensitive-touch recognition, Morse code transmission, and acoustic sound recognition. Moreover, owing to its high sensitivity in a broad pressure range, the flexible AMS pressure sensor attached to various parts of the body exhibited the capability for pulse detection, motion recognition, muscle movement detection, and voice recognition. Finally, the wireless real-time monitoring of human motion was demonstrated for practical uses, which shows the potential for promising intelligent wearable devices.

Experimental section

Preparation of LGO solution

The LGO (large-sized graphene oxide) was prepared using a modified Hummers' method. To obtain the graphite intercalation compound, 1 g of graphite (Asbury, 99.99%), 30 mL of sulfuric acid (H$_2$SO$_4$, Junsei, 95%), and 10 mL of nitric acid (HNO$_3$, Junsei, 97%) were mixed and stirred at room temperature for 12 h. The suspension was vacuum filtered and washed with 1 L of DI water, followed by drying in a vacuum oven at 60 °C for 24 h. The dry graphite intercalation compound powder was annealed at 1000 °C under a flow of 100 sccm of Ar with 600 Torr for 1 min. Then, 400 mg of expanded graphite and 92 mL of sulfuric acid were mixed and stirred for 12 h. 2.8 g of potassium permanganate (KMnO$_4$, Junsei, 99.3%) as an oxidizing agent was added to the mixture with continuous stirring in an ice bath. Then, the mixture was stirred on a hot plate at 35 °C for 2 h. After cooling the flask in an ice bath, 10 mL of DI water and 1 mL of hydrogen peroxide (H$_2$O$_2$, Junsei, 30%) were added to the mixture to terminate the oxidation reaction. The suspension was centrifuged and washed with 3 M hydrochloric acid solution (HCl, Samchun, 35%) to remove metal ions and then rinsed with DI water until the pH reached 7. Finally, the LGO was dispersed in DI water for spray coating.

Preparation of patterned Cu molds

The copper foil (Cu, Sigma-Aldrich, ≥99.8%) was coated with positive photoresist (PR, AZ 4620, AZ Electronic Materials) and exposed to UV light for 20 s using a photomask with circular arrays of radii 10, 15, 25, and 50 μm. After being developed with a developer (AZ 400K, AZ Electronic Materials), the patterned copper foil was selectively and isotropically wet-etched with a ferric chloride solution (FeCl$_3$, UN2582, TRANSENE Company, Inc.) to get a reverse-dome shape. The isotropic etching time was carefully controlled for each microdome radius to ensure reproducible reverse-dome geometries.

Preparation of LrGO/md-PDMS

Polydimethylsiloxane (PDMS, Sylgard 184) was prepared by mixing base silicone with a curing agent in a weight ratio of 10 : 1. The mixture was degassed in a vacuum chamber for 30 min to remove bubbles. Before casting PDMS, the prepared patterned mold was cleaned and coated with a release agent to facilitate easy removal of the cured PDMS from the mold. Then, the mixture was poured onto the prepared mold. After curing at 80 °C for 2 h, the microdome-textured PDMS (md-PDMS) substrate was peeled off the mold. To improve the adhesion between PDMS and LGO, the md-PDMS substrate was UV–O$_3$ treated for 3 min and immersed in 3-triethoxsilylpropylamine (APTES, Sigma-Aldrich, 99%) solution for 4 h. After surface treatment, the prepared LGO solution was spray-coated onto the md-PDMS substrate in fixed concentrations (0.5 mg mL^{-1}), spray amounts (5 mL), and spray areas with heating on a hot plate at 170 °C to minimize device-to-device variations. The coated LGO layer was chemically reduced to large-sized reduced graphene oxide (LrGO) using hydroiodic acid (HI, Junsei, 55%) for 30 min to obtain LrGO/md-PDMS.

Fabrication of pressure sensors

The LrGO/md-PDMS substrate was cut into a rectangular-shaped piece with a size of 2.5 cm × 2 cm, including the electrode pad part. Finally, the two LrGO/md-PDMS substrates were assembled face-to-face, featuring the top layer with a radius of 50 μm and the bottom layer with a radius of 10 μm. In cases with different asymmetric ratios of 3.3 and 2, the bottom layer utilized radii of 15 and 25 μm, respectively. For SMS (L) and (S) pressure sensors, the top and bottom layers were assembled with equal radii of 50 and 10 μm, respectively. The Ag sputtered md-PDMS substrates were assembled with the same radius size as the control group of AMS pressure sensors using LrGO/md-PDMS.

Characterization of materials and AMS pressure sensors

The surface morphologies of LGO sheets and LrGO/md-PDMS were characterized using a field emission scanning electron microscope (FE-SEM, Gemini 500, ZEISS). The sheet resistances of SrGO and LrGO were measured using a Hall effect measurement system equipped with 4-point probes (HMS5000, Ecopia). Also, Raman spectroscopy (NRS-5100, JASCO) investigation was carried out using a laser source with a wavelength of 532 nm to analyze the crystallinity of graphene-based samples. To evaluate the performance of the pressure sensor, electromechanical measurements were conducted using a potentiostat (VSP, BioLogic, Grenoble, France) at an operating voltage of 1 V,

This journal is © The Royal Society of Chemistry 2026

J. Mater. Chem. A, 2026, 14, 8041–8051 | 8049

while controlled weights were gently loaded onto the pressure sensor to apply pressures of up to ≈ 10 kPa. The cyclic loading test was performed using a pushing & pulling machine system (SNM-PP 200N, Withus Inc., Korea) and a digital source meter (2611A, Keithley, USA) to apply repeated normal force to the sensor. The acquired data were wirelessly transmitted from an Arduino board to a mobile application *via* Wi-Fi network connection. The experiments for the pressure sensors were performed at Pusan National University [institutional review board (IRB) approved protocol: 2018_86_HR]. All studies involving human subjects were conducted in accordance with informed consent.

Computational details

The FEM analysis was conducted using Abaqus.[56] Three different structures were modeled as a representative volume element (RVE) in a three-dimensional shape. To reduce the computational time, one-quarter of the 3D model with symmetric conditions was utilized. A linear elastic material model was applied with Young's modulus $E = 350$ kPa and Poisson's ratio $\nu = 0.48$ for PDMS.[57] Quadratic tetrahedral elements (C3D10) were adopted to mesh the three models, and the number of elements for meshing was approximately 400 000. The self-contact condition was applied to the surface of each microdome in order to consider crease localization caused by the large deformation, and the stiffness of the system was updated at every deformation increment to account for the geometric nonlinearity.

Author contributions

Yeoul Kang: conceptualization, experiments, formal analysis, data curation, writing – original draft. Mary Kim and Sangryun Lee: computational analysis, writing. Seung Geun Jo: experiments, formal analysis. Jongmoon Jang: experiments. Sang-Jin Lee: experiments. Ki Jun Yu: formal analysis, writing. Jung Woo Lee: resources, supervision, writing – review & editing.

Conflicts of interest

There are no conflicts to declare.

Data availability

Data will be made available on request.

Supplementary information (SI) is available. See DOI: https://doi.org/10.1039/d5ta05525c.

Acknowledgements

Notes and references

1 Y. Cheng, K. Wang, H. Xu, T. Li, Q. Jin and D. Cui, *Anal. Bioanal. Chem.*, 2021, **413**, 6037.

2 J. S. Meena, S. B. Choi, S.-B. Jung and J.-W. Kim, *Mater. Today Bio*, 2023, 100565.

3 E. S. Dellon, R. Mourey and A. L. Dellon, *Plast. Reconstr. Surg.*, 1992, **90**, 112.

4 R. Li, Q. Zhou, Y. Bi, S. Cao, X. Xia, A. Yang, S. Li and X. Xiao, *Sens. Actuators, A*, 2021, **321**, 112425.

5 G. Schwartz, B. C.-K. Tee, J. Mei, A. L. Appleton, D. H. Kim, H. Wang and Z. Bao, *Nat. Commun.*, 2013, **4**, 1859.

6 W.-D. Li, J.-H. Pu, X. Zhao, J. Jia, K. Ke, R.-Y. Bao, Z.-Y. Liu, M.-B. Yang and W. Yang, *J. Mater. Chem. C*, 2020, **8**, 16774.

7 J. Li, R. Bao, J. Tao, Y. Peng and C. Pan, *J. Mater. Chem. C*, 2018, **6**, 11878.

8 T. Wang, H. Yang, D. Qi, Z. Liu, P. Cai, H. Zhang and X. Chen, *Small*, 2018, **14**, 1702933.

9 T. Q. Trung and N. E. Lee, *Adv. Mater.*, 2016, **28**, 4338.

10 A. Fiorillo, C. Critello and S. Pullano, *Sens. Actuators, A*, 2018, **281**, 156.

11 H. Chang, S. Kim, S. Jin, S.-W. Lee, G.-T. Yang, K.-Y. Lee and H. Yi, *ACS Appl. Mater. Interfaces*, 2018, **10**, 1067.

12 C. L. Choong, M. B. Shim, B. S. Lee, S. Jeon, D. S. Ko, T. H. Kang, J. Bae, S. H. Lee, K. E. Byun and J. Im, *Adv. Mater.*, 2014, **26**, 3451.

13 J. Park, Y. Lee, J. Hong, Y. Lee, M. Ha, Y. Jung, H. Lim, S. Y. Kim and H. Ko, *ACS Nano*, 2014, **8**, 12020.

14 X. Cui, Y. Jiang, L. Hu, M. Cao, H. Xie, X. Zhang, F. Huang, Z. Xu and Y. Zhu, *Adv. Mater. Technol.*, 2023, **8**, 2200609.

15 L. Cheng, W. Qian, L. Wei, H. Zhang, T. Zhao, M. Li, A. Liu and H. Wu, *J. Mater. Chem. C*, 2020, **8**, 11525.

16 X. Zhang, Y. Hu, H. Gu, P. Zhu, W. Jiang, G. Zhang, R. Sun and C. P. Wong, *Adv. Mater. Technol.*, 2019, **4**, 1900367.

17 C. Yang, L. Li, J. Zhao, J. Wang, J. Xie, Y. Cao, M. Xue and C. Lu, *ACS Appl. Mater. Interfaces*, 2018, **10**, 25811.

18 C. Zhang, R. Chen, C. Xiao, H. Zhao, Y. Wang, D. Geng, S. Chen, T. Luo and W. Zhou, *Adv. Mater. Interfaces*, 2022, **9**, 2101596.

19 P. Nie, R. Wang, X. Xu, Y. Cheng, X. Wang, L. Shi and J. Sun, *ACS Appl. Mater. Interfaces*, 2017, **9**, 14911.

20 J. Shi, L. Wang, Z. Dai, L. Zhao, M. Du, H. Li and Y. Fang, *Small*, 2018, **14**, 1800819.

21 J. Li, T. Wu, H. Jiang, Y. Chen and Q. Yang, *Adv. Intell. Syst.*, 2021, **3**, 2100070.

22 S. R. A. Ruth, V. R. Feig, H. Tran and Z. Bao, *Adv. Funct. Mater.*, 2020, **30**, 2003491.

23 T. N. Tarbox, A. B. Watts, Z. Cui and R. O. Williams, *Drug Deliv. Transl. Res.*, 2018, **8**, 1828.

24 M.-Y. Liu, C.-Z. Hang, X.-F. Zhao, L.-Y. Zhu, R.-G. Ma, J.-C. Wang, H.-L. Lu and D. W. Zhang, *Nano Energy*, 2021, **87**, 106181.

8050 | *J. Mater. Chem. A*, 2026, **14**, 8041–8051

This journal is © The Royal Society of Chemistry 2026

25 U. Pierre Claver and G. Zhao, *Adv. Eng. Mater.*, 2021, **23**, 2001187.

26 L. Dong, J. Yang, M. Chhowalla and K. P. Loh, *Chem. Soc. Rev.*, 2017, **46**, 7306.

27 Q. Zheng, B. Zhang, X. Lin, X. Shen, N. Yousefi, Z.-D. Huang, Z. Li and J.-K. Kim, *J. Mater. Chem.*, 2012, **22**, 25072.

28 Y. Lv, L. Min, F. Niu, Z. Qin, M. Zhang, B. Zhao, Y. Liu and K. Pan, *Adv. Mater. Technol.*, 2023, 2201886.

29 T. H. Chang, K. Li, H. Yang and P. Y. Chen, *Adv. Mater.*, 2018, **30**, 1802418.

30 H.-I. Moon, S. Kim, J. E. Byun, Y. W. Kim, Y. W. Jung, S. G. Jo, Y. Shin, Y. Kang, S. J. Kim and E.-S. Lee, *Chem. Eng. J.*, 2023, 147819.

31 Q. Zheng, W. H. Ip, X. Lin, N. Yousefi, K. K. Yeung, Z. Li and J.-K. Kim, *ACS Nano*, 2011, **5**, 6039.

32 T. F. Emiru and D. W. Ayele, *Egypt. j. basic appl. sci.*, 2017, **4**, 74.

33 R. K. Singh, R. Kumar and D. P. Singh, *RSC Adv.*, 2016, **6**, 64993.

34 D. Cai, A. Neyer, R. Kuckuk and H. M. Heise, *J. Mol. Struct.*, 2010, **976**, 274.

35 S. Stankovich, D. A. Dikin, R. D. Piner, K. A. Kohlhaas, A. Kleinhammes, Y. Jia, Y. Wu, S. T. Nguyen and R. S. Ruoff, *Carbon*, 2007, **45**, 1558.

36 F. Tuinstra and J. L. Koenig, *J. Chem. Phys.*, 1970, **53**, 1126.

37 D. Konios, M. M. Stylianakis, E. Stratakis and E. Kymakis, *J. Colloid Interface Sci.*, 2014, **430**, 108.

38 J. Park, J. Kim, J. Hong, H. Lee, Y. Lee, S. Cho, S.-W. Kim, J. J. Kim, S. Y. Kim and H. Ko, *NPG Asia Mater.*, 2018, **10**, 163.

39 R. Holm, in: *Electric Contacts: Theory and Application*, Springer Science & Business Media, 2013.

40 J. A. Greenwood, *Br. J. Appl. Phys.*, 1966, **17**, 1621.

41 T. Zhang, Z. Li, K. Li and X. Yang, *Adv. Mater. Technol.*, 2019, **4**, 1900679.

42 S. Smocot, Z. Zhang, L. Zhang, S. Guo and C. Cao, *Nanoscale*, 2022, **14**, 17134–17156.

43 A. del Bosque, X. F. Sánchez-Romate, A. Gómez, M. Sánchez and A. Ureña, *Sens. Actuators, A*, 2023, **353**, 114249.

44 J. Shi, L. Wang, Z. Dai, L. Zhao, M. Du, H. Li and Y. Fang, *Small*, 2018, **14**, 1800819.

45 H. Li, K. Wu, Z. Xu, Z. Wang, Y. Meng and L. Li, *ACS Appl. Mater. Interfaces*, 2018, **10**, 20826–20834.

46 Y. Zhang, T. H. Chang, L. Jing, K. Li, H. Yang and P. Y. Chen, *ACS Appl. Mater. Interfaces*, 2020, **12**, 8392–8402.

47 X. Wang, Z. Feng, Y. Xia, G. Zhang, L. Wang, L. Chen, Y. Wu, J. Yang and Z. L. Wang, *Nano Energy*, 2022, **102**, 107710.

48 K. Meng, X. Xiao, W. Wei, G. Chen, A. Nashalian, S. Shen, X. Xiao and J. Chen, *Adv. Mater.*, 2022, **34**, 2109357.

49 C.-M. Huang, H.-C. Chang, S.-T. Kao, T.-C. Li, C.-C. Wei, C. Chen, Y.-T. Liao and F.-J. Chen, *Evid. Based Complement. Alternat. Med.*, 2011, **2010**, 751317.

50 S. Munir, B. Jiang, A. Guilcher, S. Brett, S. Redwood, M. Marber and P. Chowienczyk, *Am. J. Physiol. Heart Circ. Physiol.*, 2008, **294**, H1645.

51 H. Wu, H. Qi, X. Wang, Y. Qiu, K. Shi, H. Zhang, Z. Zhang, W. Zhang and Y. Tian, *J. Mater. Chem. C*, 2022, **10**, 8206.

52 H. Zhang, D. Zhang, J. Guan, D. Wang, M. Tang, Y. Ma and H. Xia, *J. Mater. Chem. C*, 2022, **10**, 15554.

53 W. Heng, S. Solomon and W. Gao, *Adv. Mater.*, 2022, **34**, 2107902.

54 Y. Zhang, B. Liu and Z. Liu, *IEEE Trans. Biomed. Circuits Syst.*, 2019, **13**, 1425.

55 M. Iizuka, M. Kobayashi, Y. Hasegawa, K. Tomita, R. Takeshima and M. Izumizaki, *J. Physiol. Sci.*, 2018, **68**, 837.

56 S. Lee, Y. Kim, J. Lee and S. Ryu, *Math. Mech. Solid*, 2019, **24**, 2944.

57 M. L. Fitzgerald, S. Tsai, L. M. Bellan, R. Sappington, Y. Xu and D. Li, *Biomed. Microdevices*, 2019, **21**, 1.

This journal is © The Royal Society of Chemistry 2026

J. Mater. Chem. A, 2026, **14**, 8041–8051 | **8051**